

Abrasive Wear Resistance of Ferrous Microstructures with Similar Bulk Hardness Levels Evaluated by a Scratch-Tester Method



BALAJI NARAYANASWAMY, ALIREZA GHADERI, PETER HODGSON, PAVEL CIZEK, QI CHAO, MOHAMMAD SAFI, and HOSSEIN BELADI

A high-strain scratch tester was employed to investigate the abrasive behavior of four different ferrous microstructures with similar bulk hardness levels. The microstructures revealed unique groove characteristics and significant deformation in their sub-surface layers. Bainite and pearlite displayed superior abrasive wear performance in comparison with martensite and tempered martensite microstructures. The characteristics of microstructure constituents were responsible for the distinct groove characteristics and material removal mechanisms. The effect of normal load was influential in the transition of the material removal mechanism from ploughing to cutting. The sub-surface layer of microstructures revealed significant deformation (*i.e.*, nanostructure formation), which was largely determined by the initial microstructure characteristics. The occurrence of work-hardening phenomenon in the sub-surface layer demonstrated a positive impact during abrasion.

<https://doi.org/10.1007/s11661-019-05354-2>

© The Minerals, Metals & Materials Society and ASM International 2019

I. INTRODUCTION

ABRASIVE wear is a predominant wear phenomenon that is observed especially in mining- and mineral-processing industries. This phenomenon takes place when a hard particle abrades a relatively softer surface resulting in severe material damage, thereby leading to a financial loss.^[1–4] In general, a tribological abrasive system is governed by two major components, namely the material (*i.e.*, microstructure) and abrasive environment characteristics. Apart from the abrasive environment, the abrasive resistance of a ferrous alloy (*i.e.*, steel) is greatly determined by a combination of its mechanical properties such as hardness, fracture toughness *etc.*, which are predominantly influenced by the metallurgical structures/phases in a steel alloy.^[5–9] Extensive studies have been reported to formulate a direct correlation between the abrasive wear resistance and the bulk hardness of ferrous microstructures.^[10–18]

However, this theory holds largely true for single-phase materials.^[19]

During the abrasive process, the microstructure characteristics progressively alter, resulting in a change in the mechanical properties.^[20–25] In general, the sub-surface layer of a ferrous alloy often experiences severe deformation leading to an increase in its hardness. This implies that the microstructure is quite dynamic in nature, and its abrasive resistance cannot be only bulk hardness dependent.^[26,27] Moreover, in the case of a multiphase microstructure, this observation is more complex as each individual metallurgical structure also play a vital role on their abrasion wear behavior.^[28] Therefore, it is essential to understand the impact of the microstructure constituents on the process of material removal during abrasion process.

One of the major drawbacks in the existing two-body abrasive wear tests (*e.g.*, pin-on-disk testing) is that the abrasive environment (*i.e.*, abrasive particle characteristics) undergoes appreciable changes (particle deterioration) during the course of a test.^[29–32] In addition, the restricted abrasive particle movement and repeated traversals of the material on the same region raises a series of arguments on the abrasive particle efficiency in two-body wear tests.^[33] This elucidates the complexities involved in existing laboratorial two-body abrasive wear tests. Consequently, this restricts the capabilities of simulating an actual industrial abrasive wear.^[34–37] Moreover, the extent of deformation and impact of an industrial abrasive action (*i.e.*, digging and excavating)

BALAJI NARAYANASWAMY is with the Institute for Frontier Materials, Deakin University, Victoria 3216, Australia and also with the Waikato Centre for Advance Materials, School of Engineering, University of Waikato, Hamilton, New Zealand. Contact e-mail: bnarayan@waikato.ac.nz ALIREZA GHADERI, PETER HODGSON, PAVEL CIZEK, QI CHAO, and HOSSEIN BELADI are with the Institute for Frontier Materials, Deakin University. MOHAMMAD SAFI is with the ArcelorMittal Hamburg GmbH, Dradenastraße 33, 21129 Hamburg, Germany.

Manuscript submitted December 10, 2018.

Article published online July 8, 2019

is very minimally replicated in the current laboratory tests.^[38] Eventually, this dictates the need for a laboratory set-up that can mimic the severity of abrasion process in terms of deformation and high loads.

To address this issue, a high-strain abrasive scratch testing was chosen for the current study, as it provided a better understanding on abrasion and the process of material removal.^[39–41] During the test, a robust indenter abraded the microstructure surface creating wear tracks (*i.e.*, grooves) under the action of a normal load. This test offered more control over the abrasive environment (*i.e.*, very limited changes in the indenter geometry during the course of the test), simulated high-strain abrasive conditions and offered better reproducibility of results. The current study investigated the abrasive behavior of bainite, pearlite, martensite and tempered martensite microstructures with similar hardness levels under the above controlled abrasive scratch test. The grooves made during the scratch test were characterized using electron microscopy and an optical profilometry. Sub-surface layers (*i.e.*, region beneath the grooves) were carefully examined to understand the abrasive response of the microstructures.

II. EXPERIMENTAL PROCEDURES

Three steel alloys with different chemical compositions were used in the current study (Table I). Different heat treatment schedules were conducted on steels I and II to obtain three distinct microstructures, namely bainite, tempered martensite and martensite. As-received ingots were initially hot-rolled in a temperature range of 1050 °C to 1100 °C to reduce their thickness to ~ 17 mm. The hot-rolled samples were then homogenized at 1250 °C for 24 hours in a controlled Argon atmosphere followed by furnace cooling. To produce a bainitic microstructure, steel I was austenitized at 1000 °C for 30 minutes, followed by an isothermal transformation at 300 °C for 5 hours in a salt bath furnace. A tempered martensitic microstructure was obtained by the process of rapid water quenching a fully austenitized steel I at 1000 °C. Then, it was subjected to the tempering treatment at 500 °C for 3 hours. Samples from steel II was austenitized at 900 °C for 5 minutes, followed by a rapid quenching in a brine solution to produce a fully martensitic microstructure. Steel III was as-received with a fully pearlitic microstructure.

Struers, Dura Scan micro-hardness machine was employed to carry out the bulk hardness measurements on the heat-treated microstructures (*i.e.*, prior to the scratch tests) at 0.01 N with a dwell time of 15 seconds. After the wear tests, the sub-surface investigations (*i.e.*, micro-hardness measurements) were also carried out along the sub-surface layer at a distance of ~ 3 μm below the sample edge. Six hardness measurements were undertaken for each sample condition and an arithmetic average was considered. Scanning electron microscope (SEM, SUPRA 55 VP FEG operated with SE2 detector at 20 kV) was extensively used for the microstructure and sub-surface characterization. For the microstructural characterization, the samples were subjected to

standard metallographic sample preparation techniques. The ground steel samples were polished in a series of polishing pads using a diamond paste of 9, 6, 3 and 1 μm successively in a Tegra-Force semi-automatic polishing unit. The samples were ultrasonically cleaned between the different stages of polishing. The immersion technique-ASTM 407^[42] was used to etch the samples using a 4 vol pct nital solution. The time required to etch the sample varied depending on the microstructure.

The abrasive resistance and the process of material removal in different microstructures were evaluated using an in-house abrasive scratch test instrument. This instrument was designed to have a controlled scratch on the surface of interest (~ 45 mm \times 55 mm \times 7 mm) using a robust indenter. The indenter was conical in shape with a spherical tip and radius of ~ 1.1 mm and was made from cemented tungsten carbide (*i.e.*, WC-10 pct Co). Similar abrasive scratch studies have been carried out using the above instrument and a more detailed operation of this set-up has also been explained elsewhere.^[43] The scratches were performed on the polished surface at a constant sliding speed of 1 mm/s, a sliding distance of 30 mm at five different normal loads, namely 200, 500, 1000, 1500 and 2000 N. The tip of the indenter was cleaned after each pass to avoid debris attachment. The instrument was interfaced with a PC, which enabled ease of control over load and displacement of the indenter.

On completion of the scratch tests, Alicona InfiniteFocus optical profilometer was employed to scan the scratch length of 30 mm at 20 times magnification for all conditions, negating ~ 2.5 mm either side of the scratch (*i.e.*, at the start and the end of the scratch). At 20 times magnification, the profilometer takes ~ 4 hours to scan one single scratch with a high step accuracy. Each wear groove profile was collected (*i.e.* average depth and width of the scratch) from one complete scan of the entire scratch (Figure 1(a)). This was specifically undertaken to understand the response of the microstructures towards an abrasive action by a normal load. Moreover, four individual sections (*i.e.*, ~ 6 mm long sections from 1 to 4, Figure 1(a)) of the 30 mm scratch were further analyzed to calculate the average volume of material loss and depth of penetration. The current study has undertaken a significant wear groove area for analysis (*i.e.* 24 mm, 6 mm \times 4) to have a reliable measurement. The volume of the material removal, V_{rem} , during the scratch test for a given condition was calculated based on the equation, $V_{\text{rem}} = [V_{\text{g}} - (V_1 + V_2)]$, where, V_{g} is the volume of the groove (mm^3), V_1 and V_2 are the volume of the built-up edges (mm^3) (Figure 1(b)). In addition, the degree of penetration, D_{p} , was determined based on the equation, $D_{\text{p}} = 2d/w$, where, d and w are the depth and width of the groove (mm)^[9] (Figure 1(b)). The surface roughness, R_{a} of the grooves was quantified based on the characteristics of the wear groove profile along the sliding direction.^[44] Average arithmetic roughness, R_{a} of the groove profile was calculated over a defined length (*i.e.*, ~ 14.5 mm) and an average was reported for all conditions.

Table I. Chemical Composition of the Steels (in Weight Percent)

Material	C	Si	Mn	Cr	Mo	Ni	Al	Co
Steel I	0.261	1.61	3.51	1.05	0.275	1.69	0.78	0.49
Steel II	0.046	0.26	1.84	0.007	0.251	0.008	0.070	0.0066
Steel III	0.844	0.27	0.67	0.02	0.006	0.04	0.002	0.004

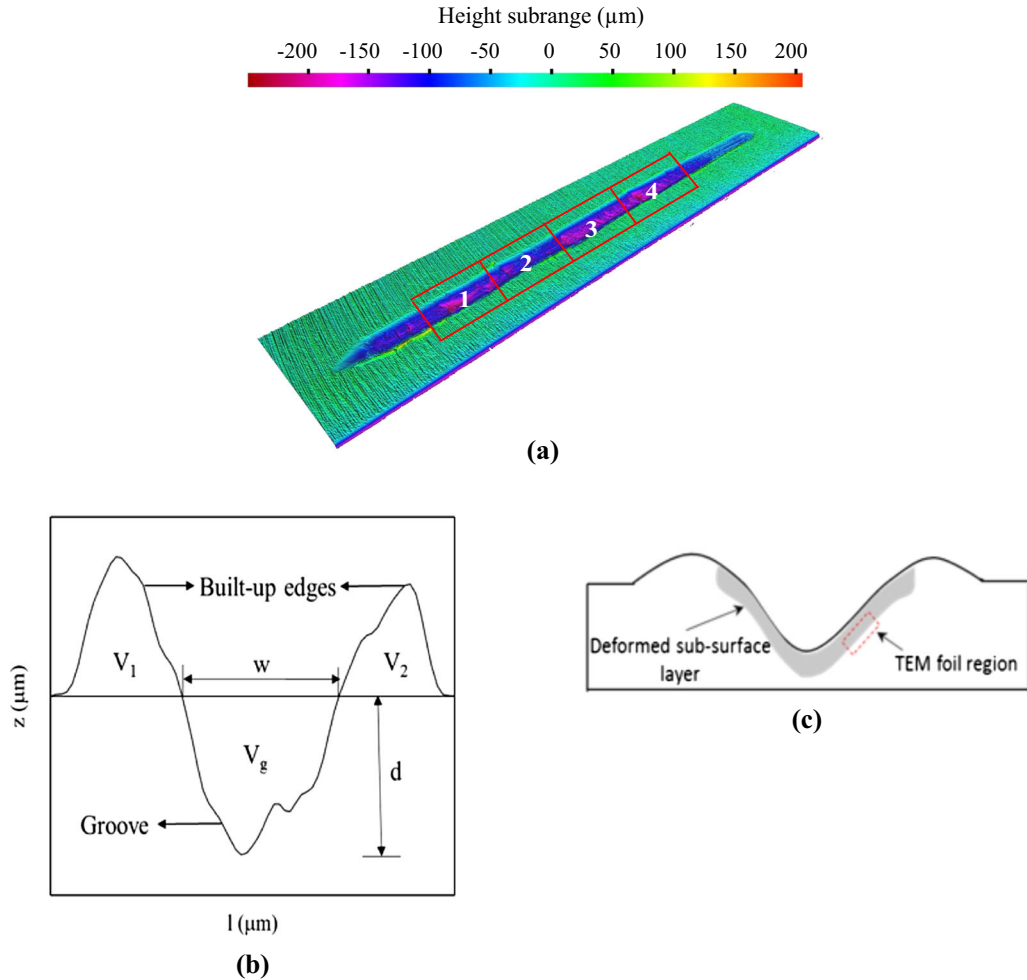


Fig. 1—(a) Topographical analysis on the wear groove of pearlite microstructure subjected to 1500 N, (b) cross-section of a scratch with built-up edges and (c) TEM foil region from the sub-surface region in schematic representation.

The sub-surface layer was further examined using electron microscopy (JEOL JEM-2100F) fitted with a NanoMEGAS ASTAR automated crystal orientation and phase mapping system. The microscope operated at 200 kV coupled with a Gatan Orius SC1000 fast-rate acquisition high-resolution camera of 11 Mpixel. The data was exported to the HKL Technology/Oxford instruments Channel 5 software for post processing. The TEM samples (*i.e.*, TEM lamellae) were prepared from the deformed regions at the sub-surface layers with a size of $\sim 6 \times 8 \mu\text{m}^2$ through Focussed Iron Beam (FIB) technique using FEI Quanta 3D FEG FIB-SEM (Figure 1(c)). This technique involved a series of precise steps namely, identifying the region of interest, platinum

deposition, bulk-out, U-cut, lift-out, mounting, thinning and cleaning.

III. RESULTS AND DISCUSSION

In this section, the impact of microstructure characteristics in a controlled highabrasive scratch testing is discussed. Specifically, the groove characteristics [*i.e.*, volume of material removal (V_{rem}), degree of penetration (D_p) and surface roughness (R_a)], scratch hardness, and sub-surface deformation layers of four different microstructures at different loading conditions were compared, analyzed and discussed.

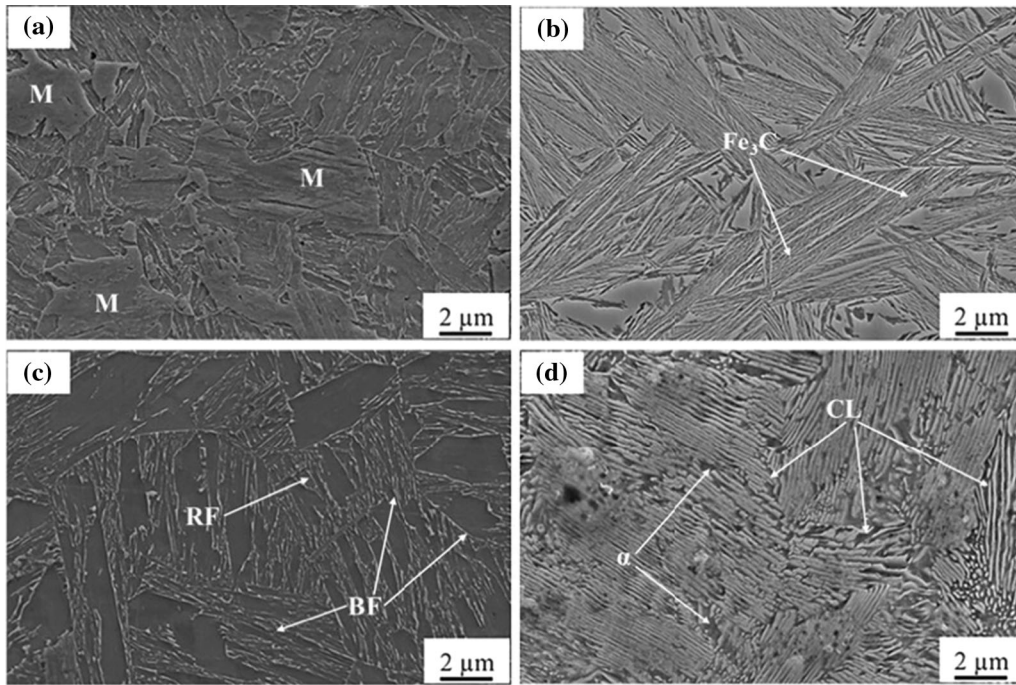


Fig. 2—SEM images of microstructures at different heat treatment conditions with similar hardness levels 330–370HV_{0.01N}: (a) Steel II—martensite, (b) Steel I—tempered martensite, (c) Steel I—bainite and retained austenite; BF bainitic ferrite, CL cementite lamellae, α ferrite.

A. Microstructural Characterization

Four distinct microstructures with similar bulk hardness levels were produced through distinctive heat treatment schedules (Figure 2). A fully martensitic microstructure consisting of highly dislocated laths was formed in steel II with a hardness level of 355 ± 3 HV_{0.01N} (Figure 2(a)). The tempered martensite microstructure formed in steel I consisted of ferritic laths with low dislocation density and cementite (*i.e.*, recovery, Figure 2(b)) with a bulk hardness of 350 ± 2 HV_{0.01N}. Isothermal transformation of steel I at 300 °C for 5 hours resulted in a bainitic microstructure with a hardness of 363 ± 1 HV_{0.01N}. The microstructure constituted of bainitic ferrite (BF) and 11.5 pct of retained austenite (RA) (Figure 2(c)). Steel III was a fully pearlitic microstructure consisting of ferrite (α) and cementite lamellae (CL), having a hardness level of 326 ± 2 HV_{0.01N} (Figure 2(d)).

B. Groove Morphology and Material Displacement

The scratches (or wear tracks) formed on the microstructures at different normal loads were topographically analyzed using an optical profilometer (Figures 3 and 4). These three-dimensional images also demonstrated that the amount of material removed from the grooves was proportional with the applied normal load. This was largely evident with an increase in the scratch depth and width (Figures 3 and 4) with increasing normal load. In general, the depth of the scratch was highest for martensite followed by tempered martensite, pearlite and bainite (Figures 3 and 4). Material displacement in martensite was observed

through the formation of step in the groove (as shown by arrows in Figures 3(b) and (c)). However, in the case of tempered martensite, this step formation was less significant than martensite microstructure and mostly observed at 2000 N (as shown by an arrow in Figure 3(f)). Meanwhile, bainite and pearlite displayed fairly shallow grooves (Figures 4(a) through (f)), *i.e.*, the depth of the grooves was relatively less in comparison with martensite and tempered martensite. This indicates a possible superior abrasive performance of bainite and pearlite microstructures.

C. Groove Profile Characterization

The scratch profiles extracted from the optical profilometry scans were plotted at different normal loads (Figure 5). As expected, the depth of the scratches increased with an increase in normal load. In addition, the material displaced to the sides (*i.e.*, built-up edges) was progressively increased to some extent, beyond which it was significantly reduced. In some cases, there was a non-uniformity in the built-up volume across the scratch edges. In the case of martensitic microstructure at 1500 N, the built-up volume on the left was substantially smaller than the built-up edge on the right in martensite microstructure (as shown by an arrow in Figure 5(a)). This trend was more dominant with an increase in the normal load, *i.e.*, > 500 N. Generally, martensite and tempered martensite microstructures exhibited wider and deeper grooves compared with bainite and pearlite for a given load condition. At lower load regimes (*i.e.*, 200 to 1000 N) bainite and pearlite microstructures displayed shallow wear grooves (*i.e.*,

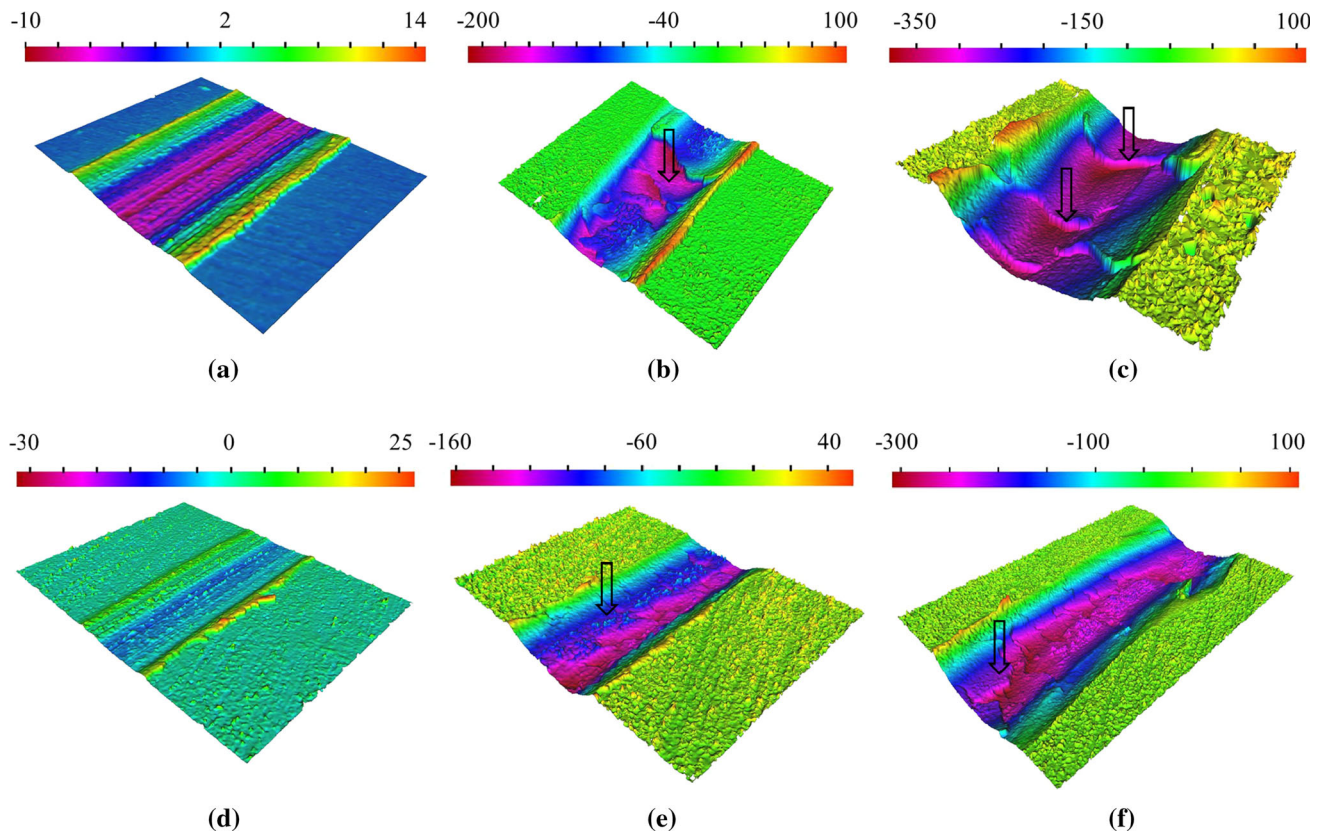


Fig. 3—Topographical analysis on the scratch tracks of martensite (a) through (c) and tempered martensite microstructures (d) through (f) subjected at different normal loads (200, 1000 and 2000 N). Note The scale bar (μm) is different for each microstructure.

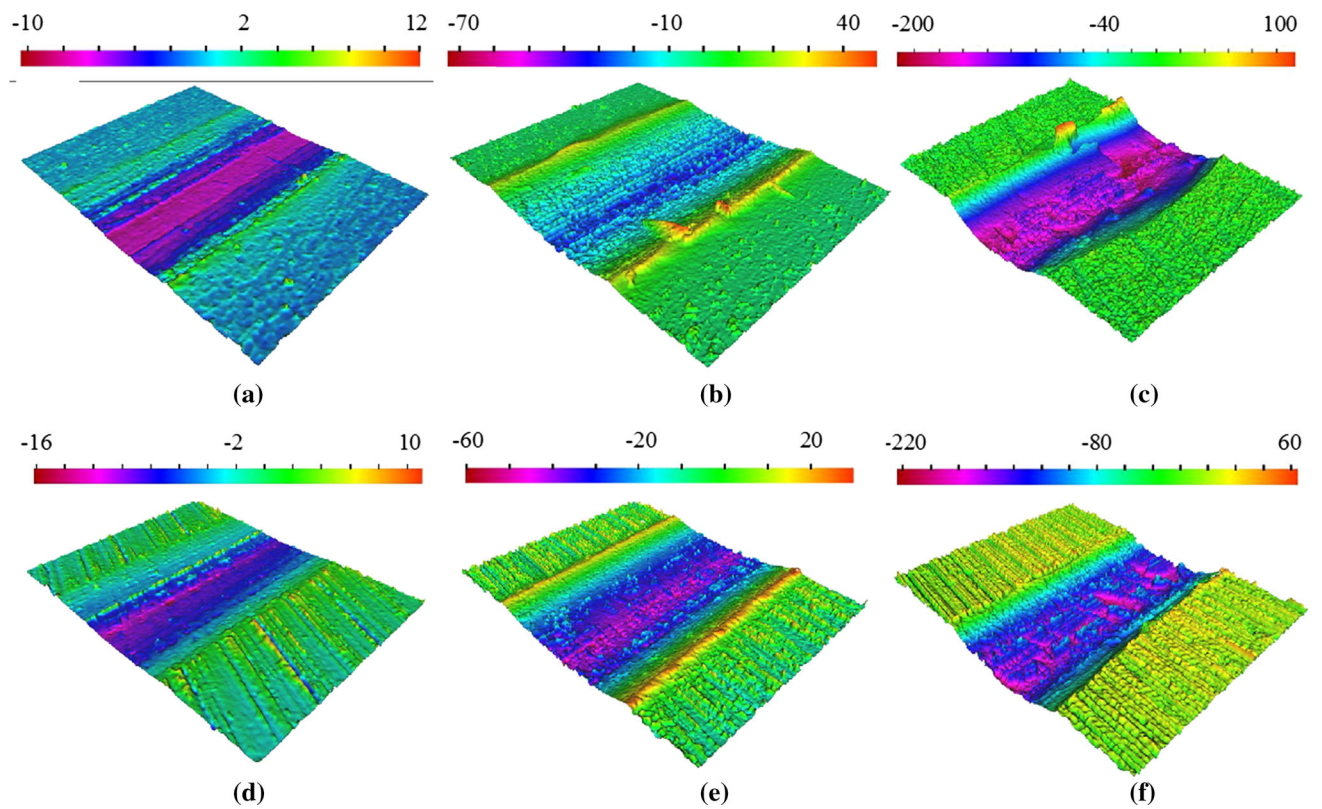


Fig. 4—Topographical analysis on the scratch tracks of bainite (a) through (c) and pearlite microstructures (d) through (f) subjected at different normal loads (200, 1000 and 1500 N). Note The scale bar (μm) is different for each microstructure.

smaller depth) indicating a lesser material loss in comparison with other microstructures. However, with an increase in the normal load (*e.g.*, 1500 N), their groove profile (*i.e.*, ~ 450 μm -width and ~ 1160 μm -depth) largely matched the groove profile (*i.e.*, ~ 450 μm -width and ~ 1250 μm -depth) of tempered martensite (Figures 5(b) through (d)) for the corresponding load. This could possibly indicate the differential abrasive behavior of microstructures with respect to the normal loading.

D. Scratch Hardness

To investigate how the materials resist during the scratch test, the scratch hardness was measured by dividing the load on the half of the projected area of the contact^[45]:

$$H_s = \frac{8F}{\pi w^2}$$

where w is the average width of the scratches and F is the normal load.

The scratch hardness values normalized by the indentation hardness were plotted as a function of load (Figure 6). As seen, unlike the indentation hardness, the scratch hardness H_s/H varied with the load, depending on the type of the microstructure. In general, the scratch

hardness H_s/H decreased with an increase in the normal load. For a given load, bainitic sample showed the highest scratch hardness followed by pearlite, tempered martensite and martensite. At the lowest load (200 N) for all microstructures, the scratch hardness values were close to the indentation hardness values, as reported elsewhere.^[45–47] However, the scratch hardness

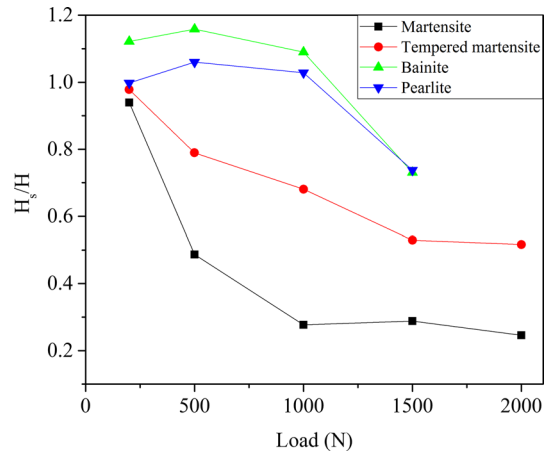


Fig. 6—Scratch hardness normalized by indentation hardness for different microstructures as a function of load.

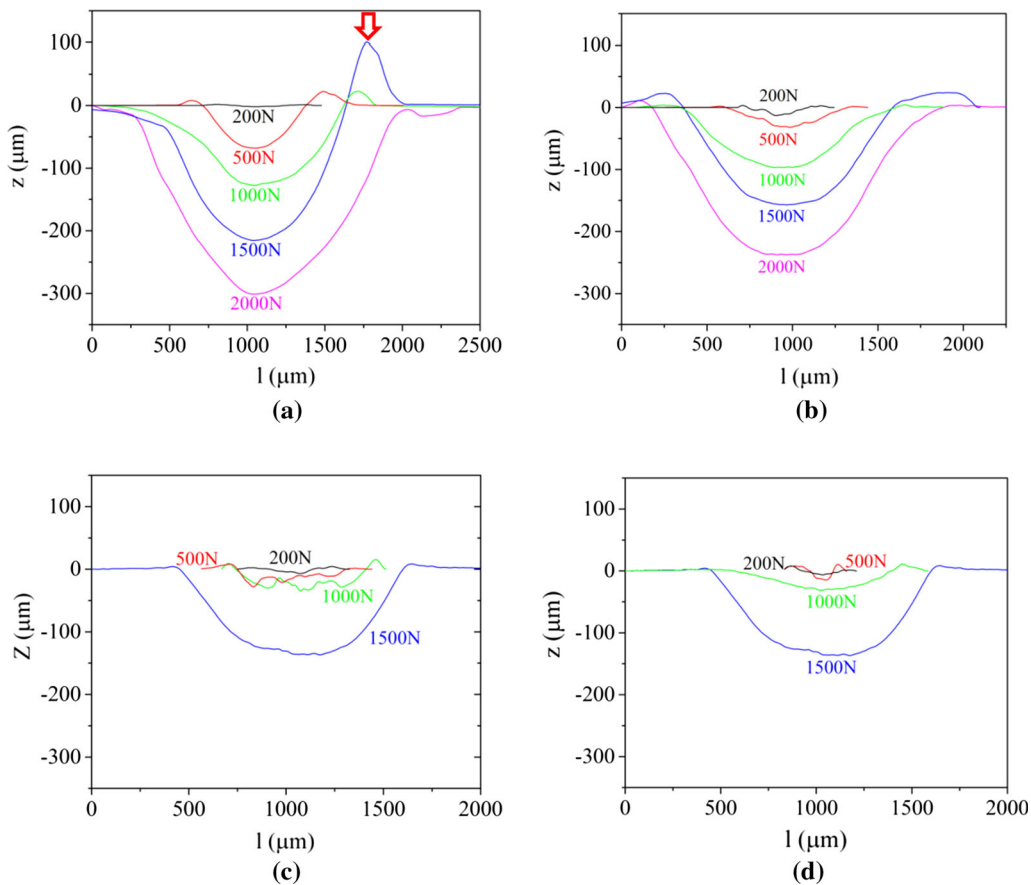


Fig. 5—A comparative groove characteristics of different microstructures as a function of the normal load: (a) martensite, (b) tempered martensite, (c) bainite and (d) pearlite.

significantly dropped with an increase in the normal load for martensite and tempered martensite microstructures. Moreover, the scratch hardness remained largely similar for bainite and pearlite microstructures up to 1000 N load and then it decreased (Figure 6). This could be attributed to the increase in the width of the scratches as the normal load increases (*i.e.*, $H_s \propto 1/w$), thereby resulting in a decrease in the scratch hardness. It is also important to note that a similar behavior with respect to the geometry of the indenter is observed elsewhere,^[41] where H_s/H values decreased with an increase in the attack angle using diamond cones with different apical angles of the indenter.

E. Material Loss

The microstructures subjected to the scratch testing were further investigated to analyse the volume of material removal, V_{rem} , and the degree of penetration, D_p , as a function of the applied normal load (Fig. 7). In general, the volume of material removal was directly proportional to the normal load for all the microstructures (Figure 7(a)). Martensite displayed the highest amount of material removal, followed by tempered martensite across different loads. However, bainite and pearlite exhibited a similar amount of material removal at all load conditions. These observations clearly confirm that the single-phase microstructures (*i.e.*, martensite and tempered martensite) exhibit a higher material loss compared with multi-phase microstructures, bainite (bainitic ferrite and retained austenite) and pearlite (ferrite and cementite lamellae, Figure 7(a)). It was interesting to note that at 1500 N, the volume of material removal of bainite and pearlite became comparable to that of tempered martensite. Moreover, this validates that bainite and pearlite had a better abrasive wear resistance at lower load regimes (*i.e.*, 200 to 1000 N, Figure 7(a)).

Additionally, the degree of penetration, D_p as a function of normal load mostly revealed a sigmoidal behavior for all microstructures, whereas for martensite, the sudden rise in the depth of penetration occurs at a

relatively lower normal load in comparison with other microstructures (Figure 7(b)). In addition, the increase in the degree of penetration was not proportional across other microstructures. In the case of tempered martensite, the degree of penetration increased from ~ 0.085 at 500 N to ~ 0.275 at 2000 N. Meanwhile, the pearlite experienced a higher degree of penetration across all loads (*i.e.*, 200 to 1500 N) compared with the bainite microstructure (Figure 7(b)). It is also important to note that the continual increase in the degree of penetration could also be attributed to an enhanced attack angle of the indenter with an increase in the normal load, thereby, resulting in the formation of deeper wear grooves and increased material loss.^[48,49]

F. Mode of Material Removal

For an in-depth understanding, the fraction of material removal (*i.e.*, $V_{rem}/V_g = f$), was plotted against D_p for all microstructures (Figure 8). The process of material removal was identified based on the value of f , *i.e.*, ploughing, $f \sim 0$ and cutting, $f \sim 1$).^[9,48] The mode of

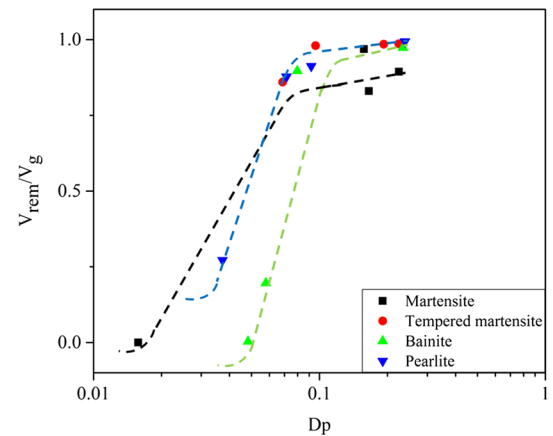


Fig. 8—Fraction of material removal, f and degree of penetration, D_p of different microstructures as a function of normal load. The dashed lines are drawn to guide the reader.

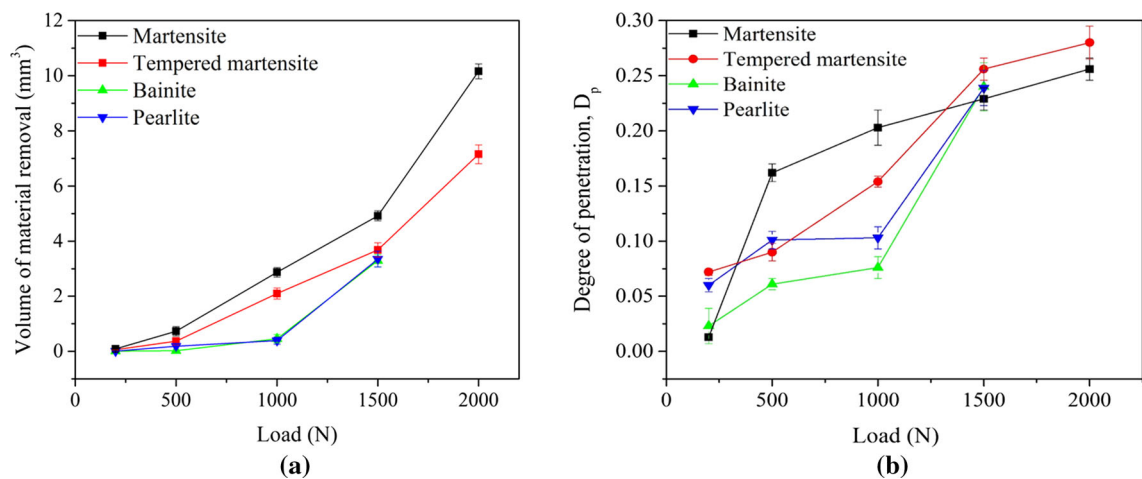


Fig. 7—(a) Volume of material removal and (b) degree of penetration in different microstructures as a function of load.

material removal (*i.e.*, cutting or ploughing) was highly dependent on the microstructure characteristics and the normal load (Figure 8). From the current study, it appears that the transition from ploughing to cutting occurs at a higher D_p value for the bainite sample in comparison with the martensite microstructure. In addition, the mode of material removal is predominantly ‘cutting’ in the case of tempered martensite microstructure. Earlier works have shown that^[50] for a given D_p value, the f value depends on the tempering condition and the bulk hardness of the ferrous microstructure. However, the process of material removal also changes for microstructures with similar hardness in this study (Figure 8). This could be attributed to the characteristics of the microstructure constituents. In other words, the combined action of brittle and ductile phases lead to a better abrasion response, *i.e.*, bainite and pearlite microstructures. Meanwhile, the martensitic microstructure offers very little resistance against the abrasion due to their brittle nature of their highly dislocated martensitic laths.^[27]

G. Groove Roughness

The average arithmetic surface roughness, R_a , was calculated along the groove for different microstructures across the load regime. Overall, the average surface roughness of the groove profile augmented with an increase in the normal load (Figure 9). Martensite and tempered martensite microstructures displayed a remarkably high R_a in comparison with bainite and pearlite microstructures. In general, the groove profile characteristics (*i.e.*, peaks and valleys) of the microstructures grew wide and deep at critical loads (*i.e.*, transition

in surface roughness—as shown by dotted boxes in Figure 9(a)). For instance, there was a steep increase in the average surface roughness, R_a , for martensite at 500 N, followed by a gradual rise with the normal load (Figure 9(b)). There was a prominent display of peaks and valleys in comparison with other microstructures (Figures 9(b) through (d)). However, in the case of tempered martensite, the steep rise was observed up to a load of 1000 N, beyond which the curve began to attain a near steady state (Figure 9(c)). The augmentation of the surface profile, *i.e.*, peaks and valleys over the transition region (*i.e.*, martensite: 200 to 500 N and tempered martensite: 500 to 1000 N) could possibly indicate the change in material removal mechanism (*i.e.*, ploughing to cutting) with respect to the normal load. For instance, ‘cutting’ wear modes are usually accompanied by higher material loss. Moreover, the mechanical properties of the displaced material (*i.e.*, deformed and brittle nature) makes them more prone to detach as wear debris. As a result, this increased material removal leads to an increase in the average surface roughness, R_a , of the groove profile for martensite and tempered martensite microstructures.

Meanwhile, bainite and pearlite microstructures revealed a gradual surface roughness increase from $\sim 2.5 \mu\text{m}$ at 200 N to $\sim 5 \mu\text{m}$ at 1000 N and then suddenly rose to $15 \mu\text{m}$ at 1500 N. This identifies a transition in the surface roughness behavior (shown by the dotted box C in Figure 9(a)) and change in material removal mechanism (ploughing to cutting) for pearlite and bainite microstructures at a relatively higher normal load in comparison with the rest of the microstructures (Figure 9(d)). This once again endorses the change in material removal mechanism with respect to normal

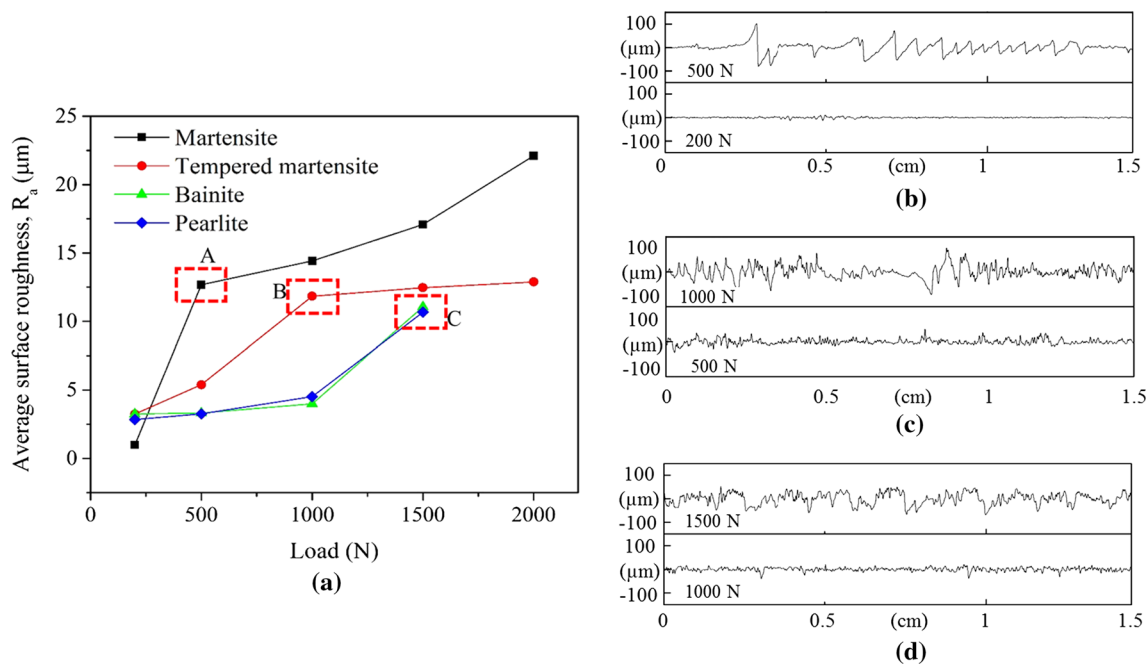


Fig. 9—(a) Average surface roughness, R_a of the scratch track in different microstructures as a function load. (b) through (d) Comparison of the groove profiles along the sliding direction at the transition loads: (b) martensite (200 to 500 N) labelled as A in (a), (c) tempered martensite (500 to 1000 N) labelled as B in (a), and (d) bainite (1000 to 1500 N) labelled as C in (a).

load and microstructure characteristics as shown earlier (Figures 4 through 8).

H. Sub-surface Characteristics

Sub-surface (*i.e.*, region beneath the grooves) analyses revealed substantial deformation in comparison with the bulk microstructure (Figure 10). The sub-surface layer is often subjected to a severe deformation during the grooving action, leading to the morphological changes (Figure 10) in the microstructure. The thickness of the sub-surface layer showed an increased dependence on the normal load applied during the scratch test (Figure 10). The severity of the abrasion (*i.e.*, high-stress) rises with an increase in the normal load, subsequently leading to an increase in the thickness of the plastically deformed sub-surface layer. It was also

observed that the hardness of the sub-surface layers increased substantially in comparison with the bulk microstructure hardness after the scratch tests. In addition, there was a progressive increase in the sub-surface layer hardness with the deformed sub-surface thickness (Fig. 11). For a given normal load condition, the bainite revealed the highest hardness value followed by the pearlite, tempered martensite and martensite microstructures.

In general, the tempered martensite and pearlite displayed the highest and lowest amount of deformation (*i.e.*, average thickness of the deformed layer) amongst all microstructures at their corresponding normal loads, respectively (as shown by the continuous and dashed lines in Figure 10). On closer examination, highly deformed sub-surface layers with fine grain structures were observed in martensite and tempered martensite

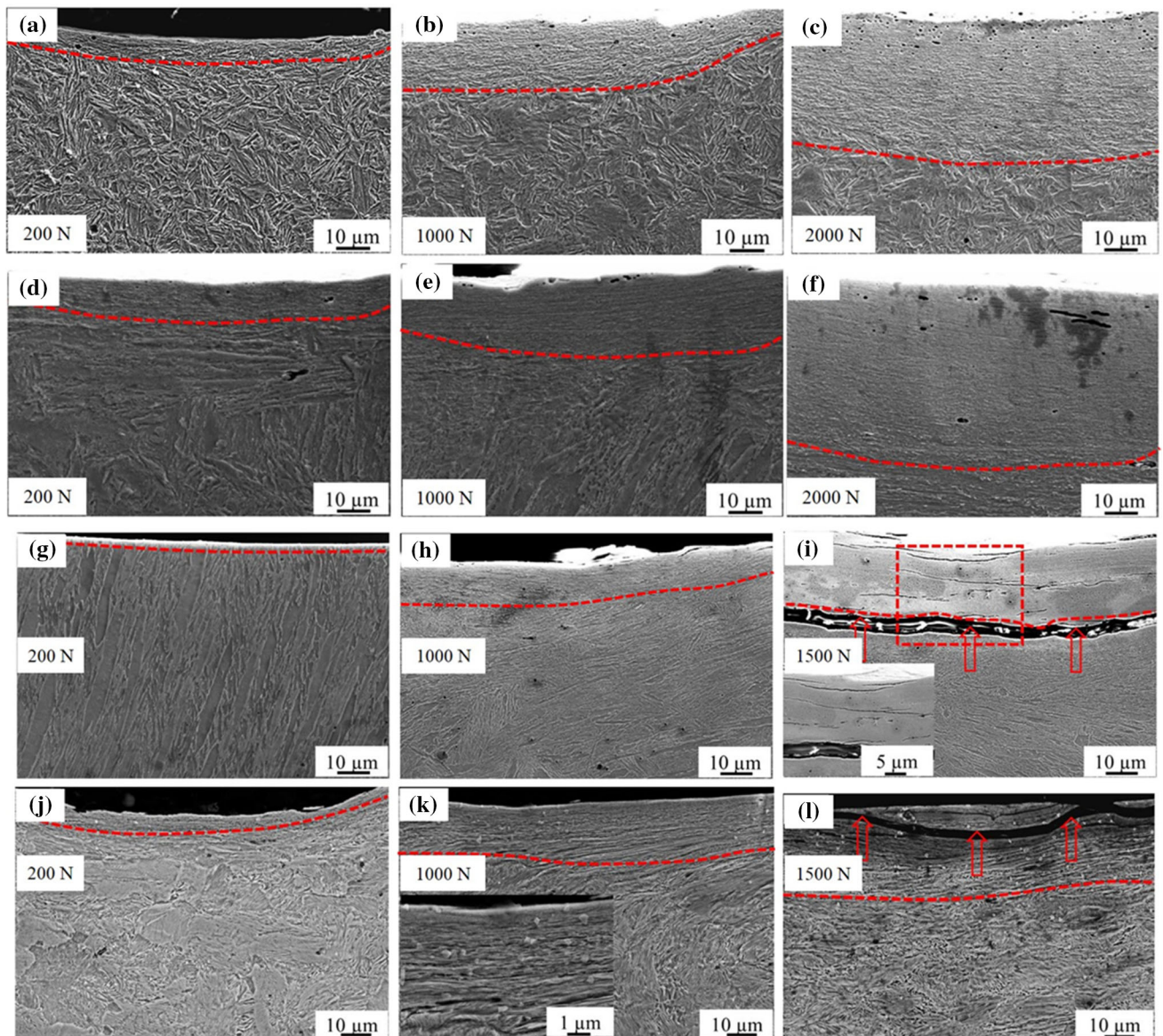


Fig. 10—Sub-surface characteristics of (a) through (c) martensite, (d) through (f) tempered martensite, (g) through (i) bainite, and (j) through (l) pearlite microstructures subjected to scratch tests.

microstructures (Figures 10(c) and (f)). In addition, porosity/inclusion (*i.e.*, black circles in Figure 10(c)) was quite severe in the case of martensite. In the case of tempered martensite, there was also a sudden increase in the sub-surface layer thickness at 1500 N, *i.e.* $\sim 22 \mu\text{m}$ at 1000 N to $\sim 53 \mu\text{m}$ at 1500 N (Fig. 11). Tempered martensite microstructure with a relatively lower dislocation density can accommodate more strain^[51] resulting in a significantly increased sub-surface hardness than martensite (Figure 11), which is quite brittle in nature.^[33] The work-hardening behavior could also be extended for the pronounced increase in the sub-surface layer thickness (*i.e.*, plastic deformation) in tempered martensite (Figures 10(a) through (f)). On the other

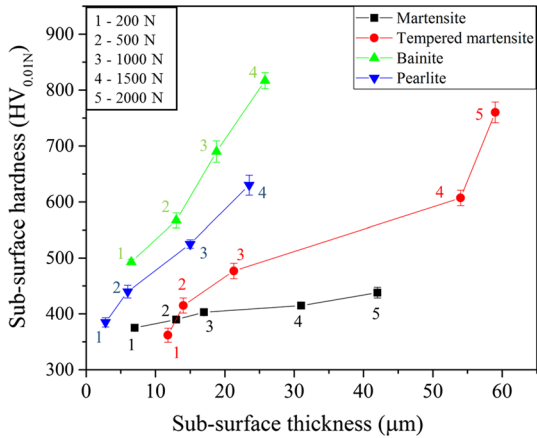


Fig. 11—Sub-surface layer thickness and hardness of different microstructures subjected to scratch tests as a function of normal load.

hand, an extensive and careful TEM characterization of the martensite sub-surface layer revealed severe deformation resulting in rows of finely segmented martensitic laths (Figure 12). These highly dislocated martensitic laths have undergone very little plastic deformation in their sub-surface layer^[52] (Figure 12), leading to minor sub-surface hardness increments (Figure 11).

The superior abrasive response of both bainite and pearlite microstructures at a load range of 200 to 1000 N (Figure 7) can also be observed through a comparatively smaller sub-surface layer thickness (Figure 11) and groove characteristics (Figures 4, 5(c) through (d), 6, 7(a), 8 and 9). At high loads, (*e.g.*, 1500 N), both bainite and pearlite displayed a distinct sub-surface layer. In the case of former, the sub-surface is a highly deformed structure (Figure 10(i)), whereas the phenomenon of microstructural realignment (*i.e.*, coalescence of ferrite and cementite regions) is dominant in the latter (Figure 10(l)). The sub-surface layers of bainite and pearlite at 1500 N, displayed signs of detachment from their bulk microstructure (as shown by arrows in Figures 10(i) and (l)). In addition, bainite displayed a highly deformed sub-surface layer that could be hardly resolved, along with several cracks propagating perpendicular to the groove direction. The presence of retained austenite in bainite (Figure 2(c)) enhances the work-hardening through the strain-induced martensitic transformation of retained austenite, so called TRansformation Induced Plasticity (TRIP) effect.^[53–58] This ultimately leads to the formation of a highly dislocated fresh martensitic region, which is in good correspondence with the paramount hardness increment (*i.e.*, bainite-125.3 pct at 1500 N) in the sub-surface layer hardness (Figure 11). In addition, the lower formability

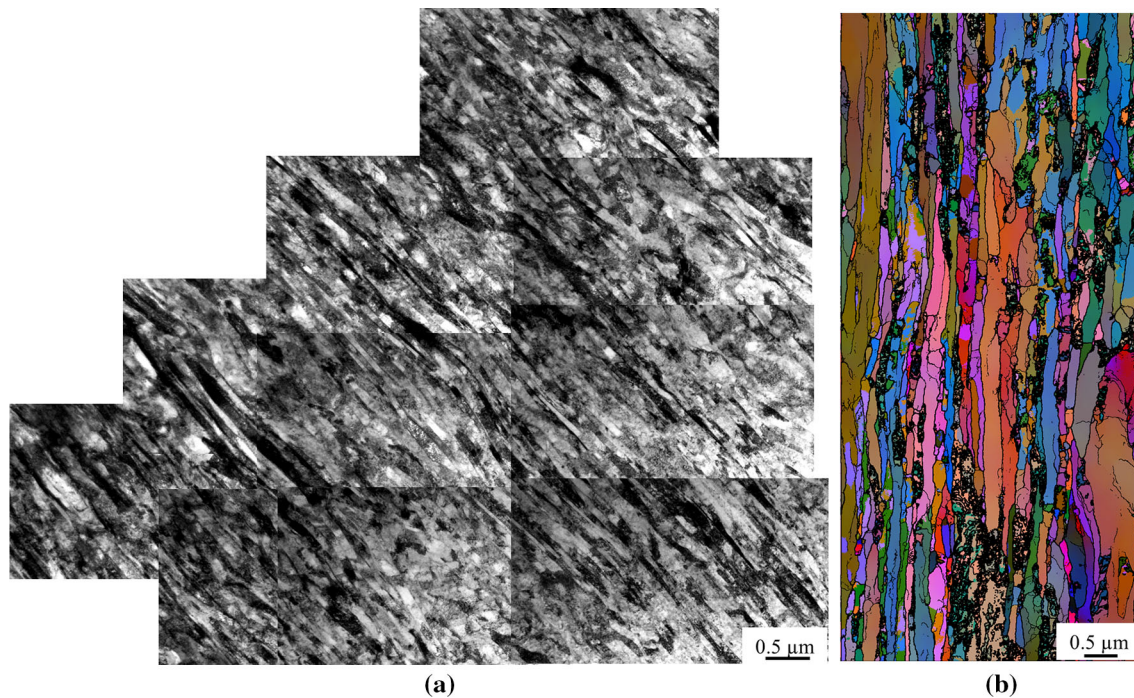


Fig. 12—(a) TEM and (b) EBSD characterization of the martensite sub-surface layer subjected to a scratch test at 2000 N.

of freshly formed martensite creates a weak bond (*i.e.*, multiple cracks along the sub-surface layer, Figure 10(i)) at the interface with the bulk microstructure. This could have resulted in the detachment of the sub-surface layer in the bainitic microstructure (Figure 10(i)).

A careful observation on the pearlite sub-surface layer revealed regions of cementite and fine ferrite grains agglomeration (Figure 13). The sub-surface layer of pearlite demonstrated a coalescence of its microstructural constituents (*i.e.*, the amalgamation of ferrite and cementite regions, Figure 10(k)) making it harder to resolve. The hard cementite lamellae offer resistance towards the penetration of the indenter and the ductile ferrite favours the realignment of lamellae. Due to the continuous strain-induced deformation during the scratch testing, the ferrite is severely work-hardened (*i.e.*, high dislocation density) and the cementite becomes fragmented into small segments in the sub-surface layer (Figure 10(k)). In addition, an augment in the ferrite dislocation density leads to an increase in its carbon solubility. Thereby, the cementite is partly dissolved into the deformed ferrite (Figure 13).^[59,60] Meanwhile, the undissolved brittle cementite particles in ferrite are vulnerable regions, leading to the formation of micro-voids that act as potential sites for the crack initiation and propagation, leading to the detachment of the sub-surface layer (Figure 10(l)). These sub-surface layer observations demonstrate the positive impact of work hardening in effecting improved abrasive wear resistance in microstructures, similar phenomena have been observed elsewhere.^[61]

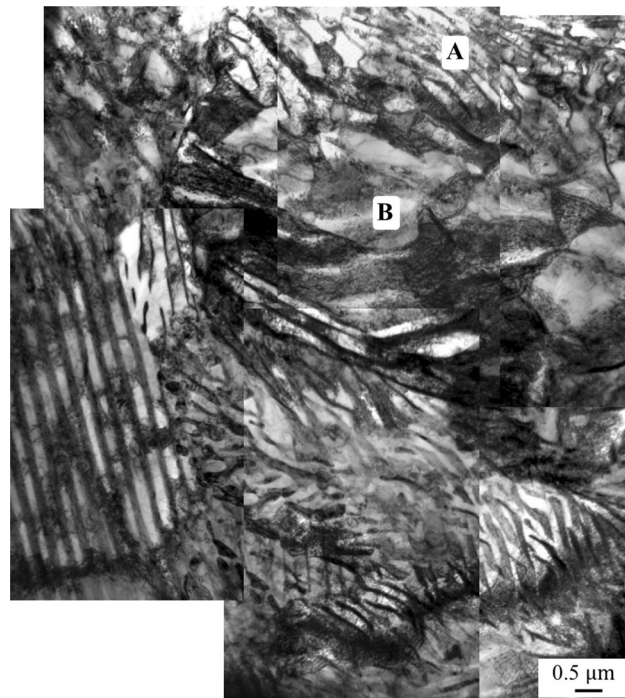


Fig. 13—TEM characterization of the pearlite sub-surface layer subjected to a scratch test at 1500 N. “A” represents cementite fragmentation region, and “B” cementite dissolution in a highly dislocated ferrite region.

Above observations and findings clearly indicate the dominant role of the microstructure characteristics, and other contributing factors such as normal load in determining their abrasive response. In the current study, the multi-phase microstructures (*i.e.*, bainite and pearlite) displayed better abrasive resistance than the single-phase microstructures (*i.e.*, martensite and tempered martensite) during a scratch test. In bainite and pearlite microstructures, the collective effort of both phases (*i.e.*, brittle and ductile) often becomes the driving force for their superior abrasive performance. Conversely, the single-phase microstructures (either brittle or ductile) appears to be more vulnerable to the abrasive action of the indenter. In addition, the abrasive behavior of the microstructures shows an increased dependence on the normal load applied during a scratch test.

IV. CONCLUSIONS

Four distinct microstructures, namely bainite, pearlite, martensite and tempered martensite with similar bulk hardness levels were subjected to a high-strain-abrasive scratch testing in this study. The grooves made during the scratch testing revealed that the abrasive behavior was greatly influenced by the microstructure characteristics and the severity of the abrasive conditions, *i.e.*, normal load. The following conclusions can be drawn from this study.

1. Generally, multiphase microstructures, *i.e.*, bainite and pearlite, displayed relatively low volume of material removal, V_{rem} , compared with the martensite and tempered martensite mostly consisting of a single phase. It should be noted, though, the bainite and pearlite had better abrasion resistance at loads lower than 1000 N.
2. The groove characteristics (*i.e.*, width, w , depth, d , scratch hardness, H_s/H and average surface roughness, R_a) of the microstructures were significantly influenced by the properties of the microstructure constituents and the normal load. Moreover, an enhanced attack angle with an increase in the load could also have contributed for a higher material loss.
3. Despite microstructures with similar bulk hardness values, their scratch hardness values were different and varied as a function of load. In addition, the critical depth of penetration, D_p , corresponding to the transition of ploughing to cutting mechanism was found to be the highest for bainite followed by pearlite, tempered martensite and martensite.
4. The distinct sub-surface characteristics of the microstructures were a clear indication of their response to the abrasive scratch test. The amount of work-hardening (*i.e.*, increase in the sub-surface hardness) had a direct and positive correlation with respect to the abrasive behavior of the microstructures.

ACKNOWLEDGMENTS

The authors would like to thank the Australian Research Council (FL0992361) for their financial support. The authors acknowledge the support of ARC mine Alloy training centre. The microstructural characterization was carried out with the help of the Deakin Advanced Characterization Facility.

REFERENCES

1. B. Bhushan: *Introduction to Tribology*, 2nd ed., Wiley, New York, 2013, pp. 328–40.
2. W.A. Glaeser, C.R. Brundle, and C.A. Evans: *Characterization of Tribological Materials*, 2nd ed., Momentum Press, New York, 2010, pp. 80–83.
3. J.A. Hawk and R.D. Wilson: *Tribology of Earthmoving, Mining, and Minerals Processing*, CRC Press LLC, Florida, 2001, pp. 1331–70.
4. I.M. Hutchings: *Tribology: Friction and Wear of Engineering Materials*, Butterworth-Heinemann Ltd, Oxford, 1992, pp. 133–35.
5. K.-H. Gahr: *Proc. Conf. Wear Mater.*, ASME, 1979, pp. 266 – 274.
6. M. Moore: *Wear*, 1974, vol. 28, pp. 59–68.
7. P. Mutton and J. Watson: *Wear*, 1978, vol. 48, pp. 385–98.
8. N. Serpik and M. Kantor: *Metalloved. Obrab. Met.*, 1958, vol. 7, pp. 46–50.
9. K.H. Zum Gahr: *Microstructure and Wear of Materials*, Elsevier Science Publishers, Amsterdam, 1987, pp. 392–417.
10. J. Larsen-Badse and K. Mathew: *Wear*, 1969, vol. 14, pp. 199–205.
11. R. Richardson: *Wear*, 1967, vol. 10, pp. 291–309.
12. M.M. Khrushov: *Proc. Conf. Lubrication and Wear*, Institution of Mechanical Engineers, 1957, pp. 655–59.
13. M.M. Khrushov: *Wear*, 1974, vol. 28, pp. 69–88.
14. M.M. Khrushov and M.A. Babichev: *Frict. Wear Mach.*, 1958, vol. 12, pp. 5–23.
15. E. Rabinowicz, L.A. Dunn, and P.G. Russel: *Wear*, 1961, vol. 4, pp. 345–55.
16. A. Misra and I. Finnie: *Wear*, 1981, vol. 68, pp. 33–39.
17. J. Larsen-Badse: *Trans. Metall. Soc.*, 1996, vol. 236, pp. 1461–66.
18. J. Larsen-Badse: *Wear*, 1968, vol. 12, pp. 357–68.
19. K. Wellinger, H. Uetz, and M. Gürleyik: *Wear*, 1968, vol. 11, pp. 173–99.
20. H. Çimenoglu: *Wear*, 1997, vol. 210, pp. 204–10.
21. N. Dube and I. Hutchings: *Wear*, 1999, vol. 233, pp. 246–56.
22. J. Larsen-Basse: *Scripta Metall. Mater.*, 1990, vol. 24, pp. 821–26.
23. S. Mezlini, M. Zidi, H. Arfa, M.B. Tkaya, and P. Kapsa: *Comptes Rendus Mec.*, 2005, vol. 333 (11), pp. 830–37.
24. O. Modi, D. Mondal, B. Prasad, M. Singh, and H. Khaira: *Mater. Sci. Eng. A*, 2003, vol. 343, pp. 235–42.
25. B. Prasad and S. Prasad: *Wear*, 1991, vol. 151, pp. 1–12.
26. S.D. Bakshi, P. Shipway, and H. Bhadeshia: *Wear*, 2013, vol. 308, pp. 46–53.
27. B. Narayanaswamy, P. Hodgson, and H. Beladi: *Wear*, 2016, vols. 354–355, pp. 41–52.
28. D. Rigney, L. Chen, M.G. Naylor, and A. Rosenfield: *Wear*, 1984, vol. 100, pp. 195–219.
29. A. Mercer and I. Hutchings: *Wear*, 1989, vol. 132, pp. 77–97.
30. A. Misra and I. Finnie: *Wear*, 1981, vol. 65, pp. 359–73.
31. M. Moore: *Wear Mater.*, 1983, pp. 1–11.
32. E. Rabinowicz and A. Mutis: *Wear*, 1965, vol. 8, pp. 381–90.
33. B. Narayanaswamy, P. Hodgson, and H. Beladi: *Wear*, 2016, vol. 354, pp. 41–52.
34. X. Xu, S. van der Zwaag, and W. Xu: *Wear*, 2017, vol. 385, pp. 106–13.
35. J.I. Pereira, G. Tressiaa, P.C. Machado, L.A. Franca, and A. Sinatora: *Tribol. Int.*, 2018, vol. 128, pp. 337–48.
36. R. Ghasemi, L. Elmquist, E. Ghassemali, K. Salomonsson, and A.E.W. Jarfors: *Tribol. Int.*, 2018, vol. 120, pp. 465–75.
37. X. Xu, S. van der Zwaag, and W. Xu: *Wear*, 2016, vol. 358, pp. 80–88.
38. T.A. Adler and R.P. Walters: *Wear*, 1993, vols. 162–164, pp. 713–20.
39. K.-H. Zum Gahr and D.V. Doane: *Metall. Trans. A*, 1980, vol. 11, pp. 613–20.
40. M. Woldman, E. Van Der Heide, T. Tinga, and M.A. Masen: *Wear*, 2013, vol. 301, pp. 76–81.
41. X. Xu, S. van der Zwaag, and W. Xu: *Wear*, 2015, vol. 322, pp. 51–60.
42. ASTM E407-07(2015)e1, Standard Practice for Microetching Metals and Alloys, ASTM International, West Conshohocken, PA, 2015. <https://www.astm.org/Standards/E407>. Accessed 9 June 2019.
43. A. Ghaderi, G. Saha, T. Guo, D. Fabijanic, and M.R. Barnett: *Wear*, 2018, vol. 404, pp. 53–165.
44. K.J. Hume: *A History of Engineering Metrology*, Mechanical Engineering Publications, London, 1980, pp. 152–56.
45. J.A. Williams: *Tribol. Int.*, 1996, vol. 29, pp. 675–94.
46. C.A. Brookes, P. Green, P.H. Harrison, and B. Moxley: *J. Phys. D*, 1972, vol. 5, pp. 1284–93.
47. T.A. Adler and R.P. Walters: *Wear*, 1993, vols. 162–164, pp. 713–20.
48. K. Hokkirigawa and K. Kato: *Wear*, 1988, vol. 21, pp. 51–57.
49. F. Pöhl, C. Hades, and W. Theisen: *Wear*, 2019, vol. 422, pp. 212–22.
50. K. Hokkirigawa and K. Kato: *Wear*, 1988, vol. 123, pp. 241–51.
51. X. Xu, S. van der Zwaag, and W. Xu: *Wear*, 2016, vol. 348, pp. 148–57.
52. X. Xu, S. van der Zwaag, and W. Xu: *Wear*, 2016, vol. 348, pp. 80–88.
53. H.K.D.H. Bhadeshia: *Bainite in Steels*, 2nd ed., Inst. of Materials, London, 1992, pp. 19–26.
54. L. Chang: *Wear*, 2005, vol. 258, pp. 730–43.
55. C. Garcia-Mateo, F. Caballero, J. Chao, C. Capdevila, and C.G. De Andres: *J. Mater. Sci.*, 2009, vol. 44, pp. 4617–24.
56. A. Leiro, A. Kankanala, E. Vuorinen, and B. Prakash: *Wear*, 2011, vol. 273, pp. 2–8.
57. B. Narayanaswamy, P. Hodgson, I. Timokhina, and H. Beladi: *Metall. Mater. Trans. A*, 2016, vol. 47A, pp. 4883–95.
58. E. Vuorinen, N. Ojala, V. Heino, C. Rau, and C. Gahm: *Tribol. Int.*, 2016, vol. 98, pp. 108–15.
59. Y.J. Li, P. Choi, C. Borchers, S. Westerkamp, S. Goto, D. Raabe, and R. Kirchheim: *Acta Mater.*, 2011, vol. 59, pp. 3965–77.
60. Y.J. Li, P. Choi, S. Goto, C. Borchers, D. Raabe, and R. Kirchheim: *Acta Mater.*, 2012, vol. 60, pp. 4005–16.
61. K. Valtonena, N. Ojalaa, O. Haikoc, and V.-T. Kuokkalaa: *Wear*, 2019, vol. 426, pp. 3–13.

Publisher's Note Springer Nature remains neutral with regard to jurisdictional claims in published maps and institutional affiliations.